# Supporting Information for "Potential vegetation changes in the permafrost areas over the Tibetan Plateau under future climate warming"

Rui Chen[1,2], Jan Nitzbon[1], Thomas Schneider von Deimling[1], Simone Maria Stuenzi[1], Ngai-Ham Chan[1], Julia Boike[1,2], and Moritz Langer[1,3]

[1]Permafrost Research Section, Alfred Wegener Institute Helmholtz Centre for Polar and Marine Research, Potsdam, Germany

[2]Geography Department, Humboldt-Universität zu Berlin, Berlin, Germany

[3]Department of Earth Sciences, Vrije Universiteit Amsterdam, Amsterdam, the Netherlands

## Contents of this file

## Text S1. Description of surface energy balance and hydrology scheme in CryoGridLite

### S1.1 The surface energy balance scheme

In comparison to the CryoGridLite model, as described in (Langer et al., 2024), where the upper boundary conditions to the heat conduction equation were set by the air temperature, the CryoGridLite version used in this study solves the surface energy balance equation to calculate the ground heat flux $Q_\mathrm{g}$ and translates it into a surface temperature $T_\mathrm{surf}$:

$$T_\mathrm{surf} = T_1 + \frac{Q_\mathrm{g} \Delta z_1}{2\, k_1} \tag{1}$$

where $T_1$ is the current temperature, $\Delta z_1$ is the thickness, and $k_1$ is the current thermal conductivity of the uppermost grid cell (soil or snow). For this, $Q_\mathrm{g}$ is calculated as the residual of the heat fluxes at the surface:

$$Q_\mathrm{g} = Q_\mathrm{net} - Q_\mathrm{h} - Q_\mathrm{e} \tag{2}$$

where $Q_\mathrm{net}$ is the net radiation, $Q_\mathrm{h}$ the sensible and $Q_\mathrm{e}$ the latent turbulent heat flux. In Eq. (2), $Q_\mathrm{net}$ is calculated from the incoming and outgoing fluxes of short- and longwave radiation:

$$Q_\mathrm{net} = S_\mathrm{in} + S_\mathrm{out} + L_\mathrm{in} + L_\mathrm{out} \tag{3}$$

where $S_{in}$ and $L_{in}$ are incoming shortwave and longwave radiation provided by the forcing data, and $S_{out}$ and $L_{out}$ are the outgoing shortwave and longwave radiation calculated by albedo and Kirchhoff's and Stefan-Boltzmann's law:

$$S_\mathrm{out} = -\alpha S_\mathrm{in} \tag{4}$$

$$L_\mathrm{out} = -\epsilon\, \sigma\, {T_\mathrm{surf}^{t-1}}^4 - (1-\epsilon) L_\mathrm{in} \tag{5}$$

with $\alpha$ the albedo and $\epsilon$ the emissivity, both depending on the surface condition (see table Table S1 for values), and $\sigma$ the Stefan-Boltzmann constant.

In Eq. (2), the turbulent fluxes are calculated according to the Monin-Obukhov similarity theory where $Q_\mathrm{h}$ and $Q_\mathrm{e}$ are parameterized based on the gradients of temperature and absolute humidity between the surface and a certain height above it. Differing from the scheme used by Westermann et al. (2016), we adopted Byun's scheme (Byun, 1990) to calculate the Obukhov stability parameter $L^\star$, using the parameterizations of the atmospheric stability functions suggested by Businger, Wyngaard, Izumi, and Bradley (1971).

Similar to Nitzbon et al. (2019), we reduced the latent heat flux $Q_\mathrm{e}$ during the snow-free season according to the availability of liquid water content ($\theta$) close to the surface:

$$Q_\mathrm{e} = \beta\, Q_\mathrm{e}^\mathrm{pot} \tag{6}$$

where the water availability factor $\beta \in [0, 1]$ is obtained by summing the following weighting factors $\Theta_*$ over the subsurface grid cells 1 to $N$:

$$\beta = \sum_{i=1}^{N} \Theta_{T_i}\, \Theta_{\theta_i}\, \Theta_{z_i} \tag{7}$$

where

$$\Theta_{T_i} = \begin{cases} 1 & \text{if } T_i > 0°\mathrm{C} \\ 0 & \text{else,} \end{cases} \tag{8}$$

$$\Theta_{\theta_i} = \begin{cases} 1 & \text{if } \theta_i > \theta_\mathrm{fc} \\ 0.25 \left(1 - \cos\left(\frac{\pi \theta_i}{\theta_\mathrm{fc}}\right)\right)^2 & \text{else,} \end{cases} \tag{9}$$

$$\Theta_{z_i} = \frac{e^{-\frac{z_i}{d_\mathrm{E}}} \Delta z_i}{\sum_i e^{-\frac{z_i}{d_\mathrm{E}}} \Delta z_i} \tag{10}$$

Here $\Theta_{T_i}$ ensures that only unfrozen grid cells are considered, $\Theta_{\theta_i}$ reduces the water availability if the liquid water content is below field capacity $\theta_\mathrm{fc}$, and $\Theta_{z_i}$ is a depth-weighting according to the evaporation depth $d_\mathrm{E}$ and the denominator a normalization such that $\beta \in [0, 1]$.

### S1.1 The surface energy balance scheme

In this tailored version of the CryoGridLite model, we largely followed (Nitzbon et al., 2019) to incorporate a simple 'bucket' scheme to calculate the dynamics of soil water content. The hydrology scheme is run at the hourly timestep ($\Delta t = 1\,\text{hour}$) of the model and only in the absence of a snowpack. First, the potential water to be infiltrated into or removed from the soil column ($\Delta I$ (m)) is determined by taking the difference between rainfall ($P_{\text{rain}}$) and evapotranspiration.

$$\Delta I = P_{\text{rain}} \Delta t - \frac{Q_e \, \Delta t}{\rho_{\text{w}} \, L_{\text{sl}}} \tag{11}$$

If $\Delta I > 0$, the distribution of soil water content along the vertical soil profile is derived from the infiltration process under the influence of gravity: if the water content in a cell exceeds the given value of maximum water content, the water is routed to the layer below until it eventually reaches a frozen grid cell. If there is still excess water present, the soil layers will commence saturation from the bottom upwards. In scenarios where excess water remains even after completely saturating the pore space of soil, it is then removed as surface runoff.

If $\Delta I < 0$, soil water is successively removed in a similar procedure, by reducing the water content to at least a residual water content ($\theta_{\text{rs}}$) starting from the first subsurface layer and continuing downwards until the water deficit is applied.

## References

Businger, J. A., Wyngaard, J. C., Izumi, Y., & Bradley, E. F. (1971). Flux-profile relationships in the atmospheric surface layer. *Journal of the Atmospheric Sciences*, *28*, 181–189. doi: https://doi.org/10.1175/1520-0469(1971)028⟨0181:FPRITA⟩2.0.CO;2

Byun, D. W. (1990). On the analytical solutions of flux-profile relationships for the atmospheric surface layer. *Journal of Applied Meteorology and Climatology*, *29*, 652–657. doi: https://doi.org/10.1175/1520-0450(1990)029⟨0652:OTASOF⟩2.0.CO;2

Chang, Y., Lyu, S., Luo, S., Li, Z., Fang, X., Chen, B., ... Chen, S. (2018). Estimation of permafrost on the tibetan plateau under current and future climate conditions using the cmip5 data. *International Journal of Climatology*, *38*, 5659–5676. doi: https://doi.org/10.1002/joc.5770

Chen, H., Nan, Z., Zhao, L., Ding, Y., Chen, J., & Pang, Q. (2015). Noah modelling of the permafrost distribution and characteristics in the west kunlun area, qinghai-tibet plateau, china. *Permafrost and Periglacial Processes*, *26*, 160–174. doi: https://doi.org/10.1002/ppp.1841

Chen, J., Zhao, L., Sheng, Y., Li, J., Wu, X., Du, E., ... Pang, Q. (2016). Some characteristics of permafrost and its distribution in the gaize area on the qinghai-tibet plateau, china. *Arctic, Antarctic, and Alpine Research*, *48*, 395–409. doi: https://doi.org/10.1657/AAAR0014-023

Cuo, L., Zhang, Y., & Li, N. (2022). Historical and future vegetation changes in the degraded frozen soil and the entire tibetan plateau and climate drivers. *Journal of Geophysical Research: Biogeosciences*, *127*, e2022JG006987. doi: https://doi.org/

10.1029/2022JG006987

Dai, L., Che, T., Xie, H., & Wu, X. (2018). Estimation of snow depth over the qinghai-tibetan plateau based on amsr-e and modis data. *Remote Sensing*, *10*, 1989. doi: https://doi.org/10.3390/rs10121989

Gao, Y., Luo, D., Chen, F., Lei, W., & Jin, H. (2023). Characteristics of the thermal regime and freeze-thaw cycles on the ground surface in permafrost regions in the headwater area of the yellow river. *Acta Geographica Sinica*, *78*, 604–619. doi: https://geog.com.cn/EN/10.11821/dlxb202303007

Guo, D., & Wang, H. (2013). Simulation of permafrost and seasonally frozen ground conditions on the tibetan plateau, 1981–2010. *Journal of Geophysical Research: Atmospheres*, *118*, 5216–5230. doi: https://doi.org/10.1002/jgrd.50457

Guo, D., & Wang, H. (2016). Cmip5 permafrost degradation projection:a comparison among different regions. *Journal of Geophysical Research: Atmospheres*, *121*, 4499–4517. doi: https://doi.org/10.1002/2015JD024108

Ji, F., Fan, L., Kuang, X., Li, X., Cao, B., Cheng, G., ... Zheng, C. (2022). How does soil water content influence permafrost evolution on the qinghai-tibet plateau under climate warming? *Environmental Research Letters*, *17*, 064012. doi: https://doi.org/10.1088/1748-9326/ac6c9a

Langer, M., Nitzbon, J., Groenke, B., Assmann, L.-M., von Deimling, T. S., Stuenzi, S. M., & Westermann, S. (2024). The evolution of arctic permafrost over the last 3 centuries from ensemble simulations with the cryogridlite permafrost model. *The Cryosphere*, *18*, 363–385. doi: https://doi.org/10.5194/tc-18-363-2024

Li, H., Pan, X., Washakh, R. M. A., & Nie, X. (2024). A new method of diagnosing

the historical and projected changes in permafrost on the tibetan plateau. *Earth's Future*, *12*, e2023EF003897. doi: https://doi.org/10.1029/2023EF003897

Li, R., Zhang, M., Andreeva, V., Pei, W., Zhou, Y., Misailov, I., & Basharin, N. (2023). Impact of climate warming on permafrost changes in the qinghai-tibet plateau. *Cold Regions Science and Technology*, *205*, 103692. doi: https://doi.org/10.1016/j.coldregions.2022.103692

Lu, Q., Zhao, D., & Wu, S. (2017). Simulated responses of permafrost distribution to climate change on the qinghai–tibet plateau. *Scientific Reports*, *7*, 3845. doi: https://doi.org/10.1038/s41598-017-04140-7

Luo, D., Jin, H., Jin, X., He, R., Li, X., Muskett, R. R., ... Romanovsky, V. E. (2018). Elevation-dependent thermal regime and dynamics of frozen ground in the bayan har mountains, northeastern qinghai-tibet plateau, southwest china. *Permafrost and Periglacial Processes*, *29*, 257–270. doi: https://doi.org/10.1002/ppp.1988

Mu, C., & Peng, X. (2022). *A synthesis dataset of frozen ground and soil carbon in heihe river basin qilian mountainous (2011–2020).* National Tibetan Plateau Data Center. doi: https://doi.org/10.11888/Cryos.tpdc.272840

Ni, J., Wu, T., Zhu, X., Hu, G., Zou, D., Wu, X., ... Yang, C. (2021). Simulation of the present and future projection of permafrost on the qinghai-tibet plateau with statistical and machine learning models. *Journal of Geophysical Research: Atmospheres*, *126*, e2020JD033402. doi: https://doi.org/10.1029/2020JD033402

Nitzbon, J., Langer, M., Westermann, S., Martin, L., Aas, K. S., & Boike, J. (2019). Pathways of ice-wedge degradation in polygonal tundra under different hydrological conditions. *The Cryosphere*, *13*, 1089–1123. doi: https://doi.org/10.5194/tc-13-1089

-2019

Qin, Y., Wu, T., Zhao, L., Wu, X., Li, R., Xie, C., ... Hao, J. (2017). Numerical modeling of the active layer thickness and permafrost thermal state across qinghai-tibetan plateau. *Journal of Geophysical Research: Atmospheres*, *122*, 11604–11620. doi: https://doi.org/10.1002/2017JD026858

Ran, Y., Cheng, G., Dong, Y., Hjort, J., Lovecraft, A. L., Kang, S., ... Li, X. (2022). Permafrost degradation increases risk and large future costs of infrastructure on the third pole. *Communications Earth & Environment*, *3*, 238. doi: https://doi.org/10.1038/s43247-022-00568-6

Ran, Y., Li, X., & Cheng, G. (2018). Climate warming over the past half century has led to thermal degradation of permafrost on the qinghai–tibet plateau. *The Cryosphere*, *12*, 595–608. doi: https://doi.org/10.5194/tc-12-595-2018

Ran, Y., Li, X., Cheng, G., Nan, Z., Che, J., Sheng, Y., ... Wu, X. (2021). Mapping the permafrost stability on the tibetan plateau for 2005–2015. *Science China Earth Sciences*, *64*, 62–79. doi: https://doi.org/10.1007/s11430-020-9685-3

Shen, T., Jiang, P., Ju, Q., Yu, Z., Chen, X., Lin, H., & Zhang, Y. (2023). Changes in permafrost spatial distribution and active layer thickness from 1980 to 2020 on the tibet plateau. *Science of The Total Environment*, *859*, 160381. doi: https://doi.org/10.1016/j.scitotenv.2022.160381

Wang, W., Yang, K., Zhao, L., Zheng, Z., Lu, H., Mamtimin, A., ... Moore, J. C. (2020). Characterizing surface albedo of shallow fresh snow and its importance for snow ablation on the interior of the tibetan plateau. *Journal of Hydrometeorology*, *21*, 815–827. doi: https://doi.org/10.1175/JHM-D-19-0193.1

Westermann, S., Langer, M., Boike, J., Heikenfeld, M., Peter, M., Etzelmüller, B., & Krinner, G. (2016). Simulating the thermal regime and thaw processes of ice-rich permafrost ground with the land-surface model cryogrid3. *Geoscientific Model Development*, *9*, 523–546. doi: https://doi.org/10.5194/gmd-9-523-2016

Wu, Q., Zhang, T., & Liu, Y. (2020). Thermal state of the active layer and permafrost along the qinghai-xizang (tibet) railway from 2006 to 2010. *The Cryosphere*, *31*, 417–428. doi: https://doi.org/10.1002/ppp.2059

Wu, X., Nan, Z., Zhao, S., Zhao, L., & Cheng, G. (2018). Spatial modeling of permafrost distribution and properties on the qinghai-tibet plateau. *Permafrost and Periglacial Processes*, *29*, 86–99. doi: https://doi.org/10.1002/ppp.1971v

Xu, X., & Wu, Q. (2021). Active layer thickness variation on the qinghai-tibetan plateau: Historical and projected trends. *Journal of Geophysical Research: Atmospheres*, *126*, e2021JD034841. doi: https://doi.org/10.1029/2021JD034841

Yin, G., Niu, F., Lin, Z., Luo, J., & Liu, M. (2021). Data-driven spatiotemporal projections of shallow permafrost based on cmip6 across the qinghai–tibet plateau at 1 $km^2$ scale. *Advances in Climate Change Research*, *12*, 814—827. doi: https://doi.org/10.1016/j.accre.2021.08.009

Zhang, G., Nan, Z., Hu, N., Yin, Z., Zhao, L., Cheng, G., & Mu, C. (2022). Qinghai-tibet plateau permafrost at risk in the late 21st century. *Earth's Future*, *10*, e2022EF002652. doi: https://doi.org/10.1029/2022EF002652

Zhang, W., Ren, Z., Yao, L., Zhou, C., & Zhu, Y. (2016). Numerical modeling and prediction of future response of permafrost to different climate change scenarios on the qinghai–tibet plateau. *International Journal of Digital Earth*, *9*, 442–456. doi:

https://doi.org/10.1080/17538947.2015.1041431

Zhang, Z., Wu, Q., Jiang, G., Gao, S., Chen, J., & Liu, Y. (2020). Changes in the permafrost temperatures from 2003 to 2015 in the qinghai-tibet plateau. *Cold Regions Science and Technology*, *169*, 102904. doi: https://doi.org/10.1016/j.coldregions.2019.102904

Zhao, L., Zou, D., Hu, G., Wu, T., Du, E., Liu, G., ... Cheng, G. (2021). A synthesis dataset of permafrost thermal state for the qinghai–tibet (xizang) plateau, china. *Earth System Science Data*, *13*, 4207–4218. doi: https://doi.org/10.5194/essd-13-4207-2021

Zou, D., Zhao, L., Sheng, Y., Chen, J., Hu, G., Wu, T., ... Cheng, G. (2017). A new map of permafrost distribution on the tibetan plateau. *The Cryosphere7*, *11*, 2527–2542. doi: https://doi.org/10.5194/tc-11-2527-2017

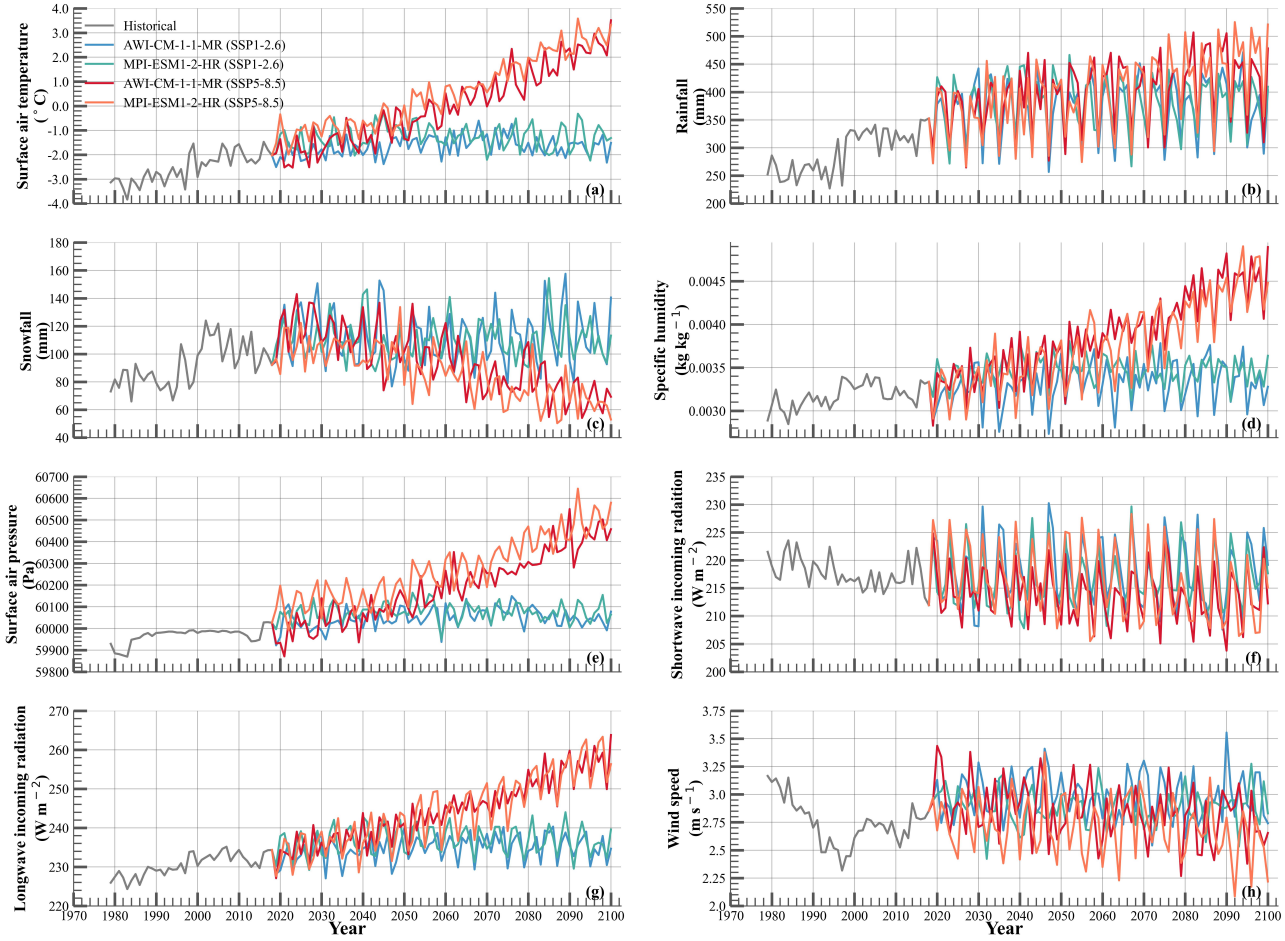


**Figure S1.** Timeseries of forcing variables (surface air temperature (a), rainfall (b), snowfall (c), specific humidity, surface air pressure (d), incoming shortwave radiation (e), incoming longwave radiation (f), and wind speed (g)) during 1979–2100 over the Tibetan Plateau under two different scenarios and two Global Climate Models.

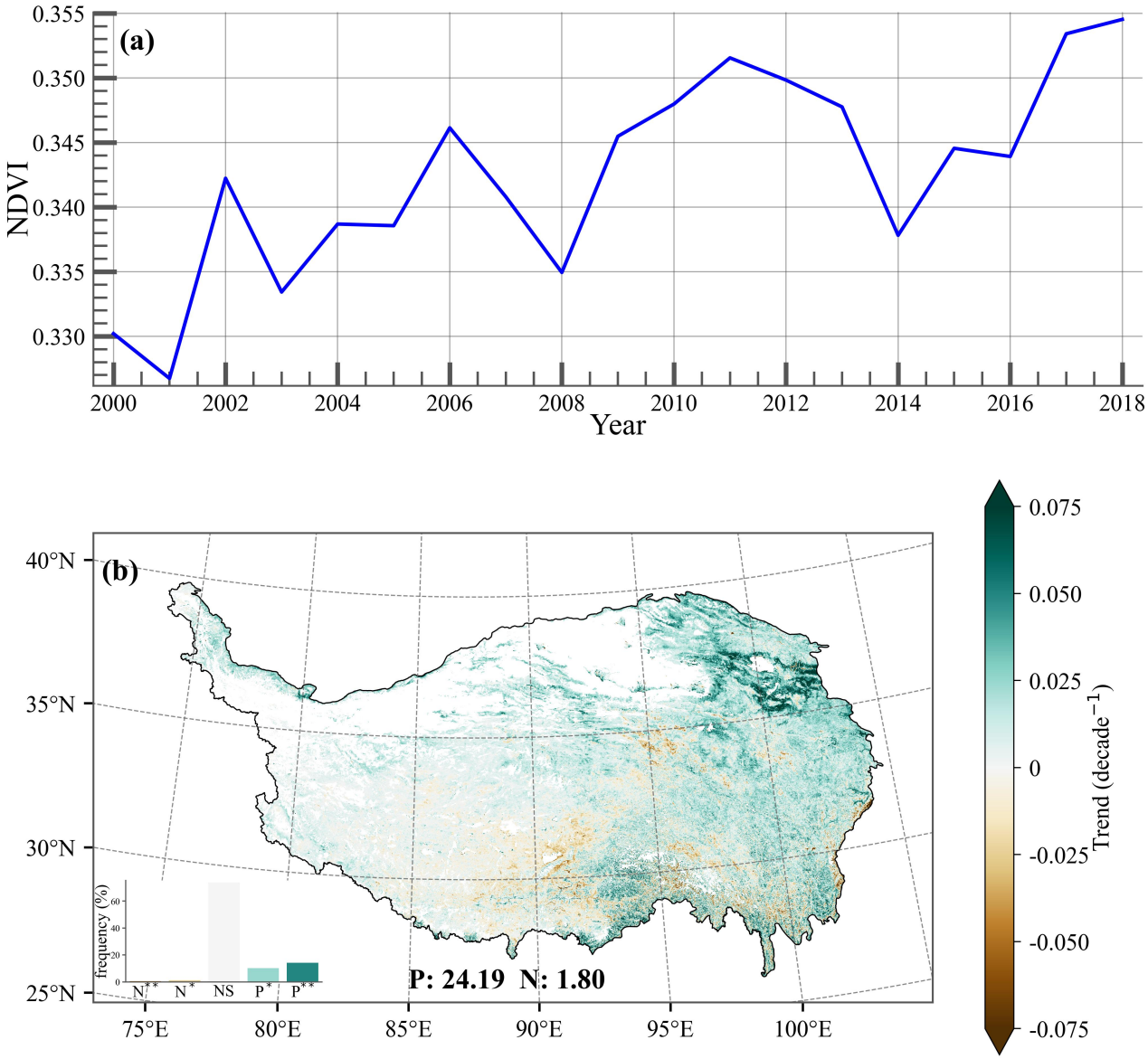


**Figure S2.** Spatiotemporal patterns of the changes of the growing season (May to September) NDVI on the Tibetan Plateau at 1km$^2$ from MODIS satellite imagery. (a) Time evolution of the growing season NDVI on the Tibetan Plateau. (b) spatial distribution of the trend of the growing season NDVI on the Tibetan Plateau. The sub-barplot represents the percentage of the number of grid cells of NDVI in each significant level to the total number of grid cells. N, NS, and P indicate negative, non-significant, and positive trends, respectively. $*$ and $**$ represent significance at p-value $\leq$0.05 and $\leq$0.01, respectively.

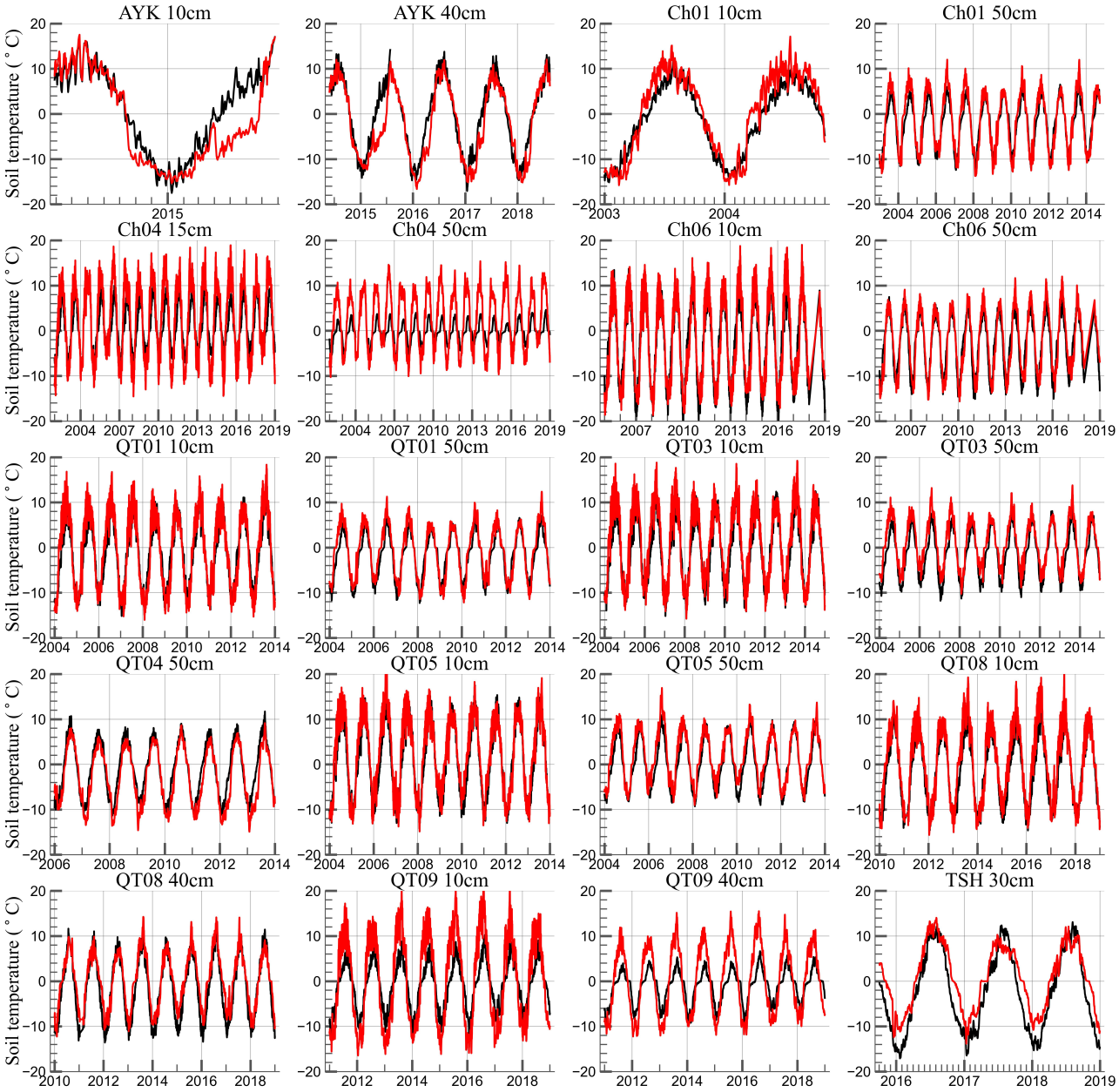


**Figure S3.** Comparison of the simulated and observed soil temperature in the upper soil layer (above 50cm). Observed soil temperature derived from Zhao et al. (2021).

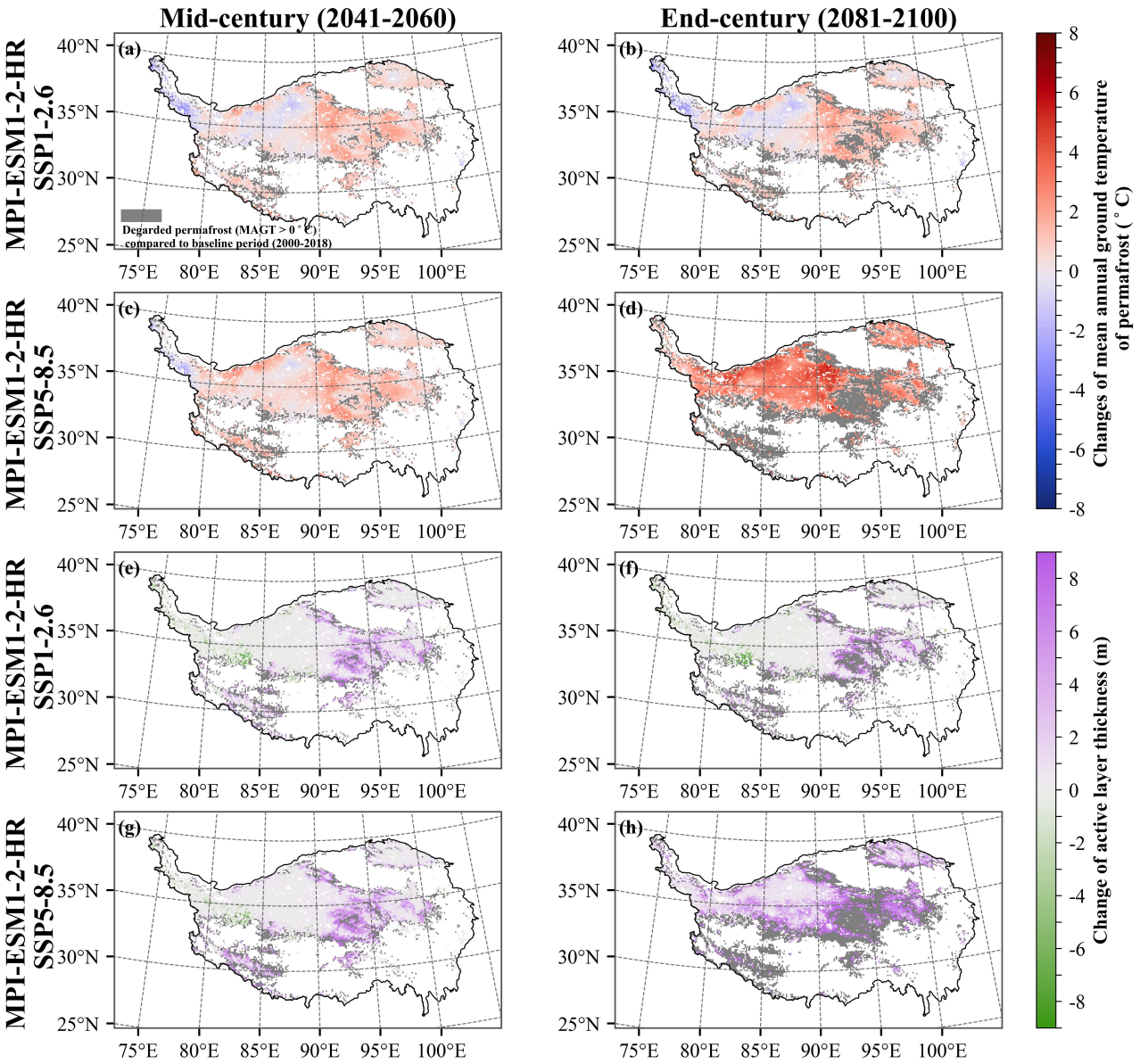


**Figure S4.** Spatial changes of the mean annual ground temperature (a-d) and active layer thickness (e-h) on the Tibetan Plateau by mid-century (2041–2060) and end-century(2081–2100) under SSP1–2.6 and SSP5–8.5 scenarios from MPI-ESM1-2-HR, related to the baseline period (2000–2018), respectively.

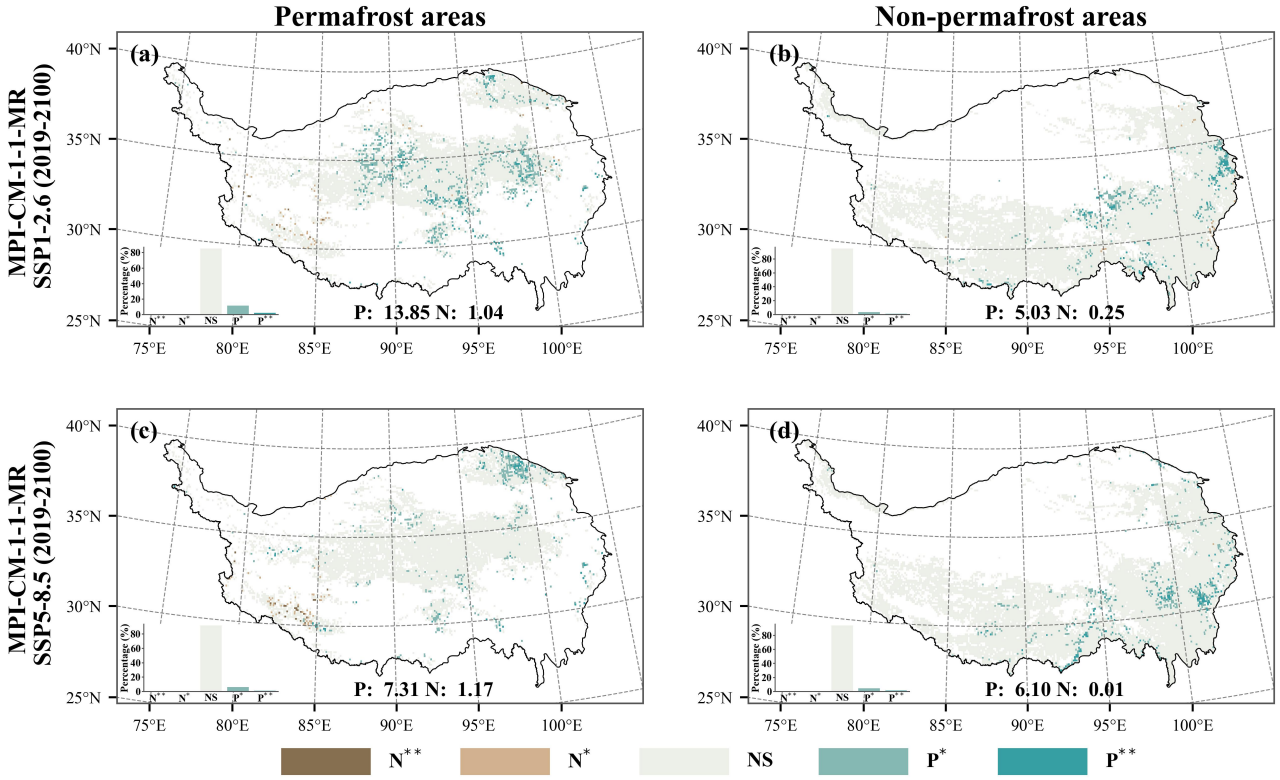


**Figure S5.** Spatial patterns of annual $NDVI_{GS}$ trend across the permafrost areas during the historical (2000–2018) and future periods (2019–2050) from MPI-ESM1-2-HR. N, NS, and P indicate negative, non-significant, and positive trends. * and ** represent significance at p-value $< 0.05$ and 0.01, respectively.

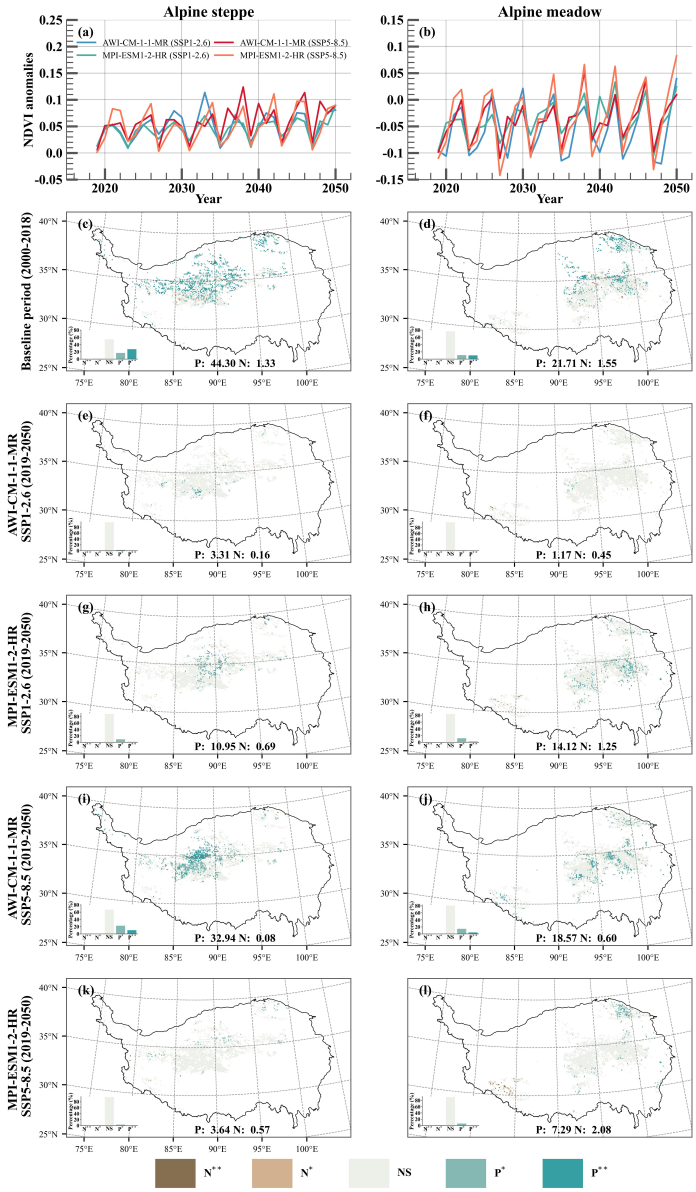


**Figure S6.** (a-b) Time series of annual NDVI$_{GS}$ anomalies (minus the mean value from 2000–2018) from 2019 to 2050 under the future climate conditions on the alpine meadow and alpine steppe on the permafrost areas over the Tibetan Plateau. The blue, red, green, and orange lines represent SSP1–2.6 and SSP5–8.5 scenarios from AWI-CM-1-1-MR and MPI-ESM1-2-HR, respectively. (c-l) Spatial patterns of annual NDVI$_{GS}$ trend during the historical (2000–2018) and future periods (2019–2050) under different climate scenarios from AWI-CM-1-1-MR and MPI-ESM1-2-HR. N, NS, and P indicate negative, non-significant, and positive trends. * and ** represent significance at p-value $< 0.05$ and 0.01, respectively.

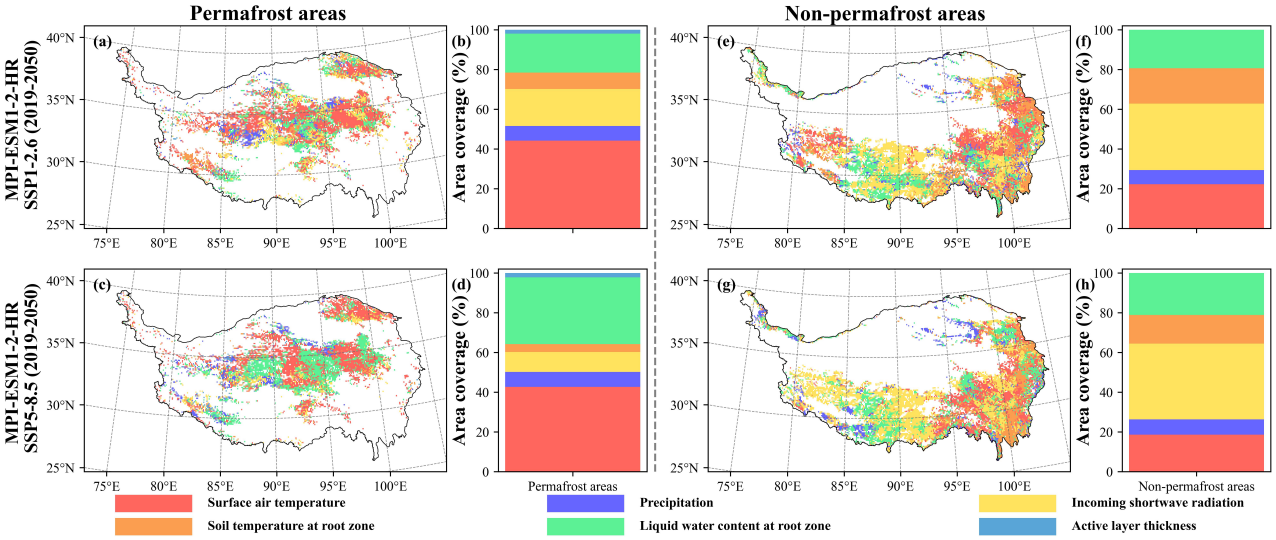


**Figure S7.** Spatial distribution of the dominant factors to the $NDVI_{GS}$ changes over different periods in the permafrost and non-permafrost areas. (a-d) Future period (SSP1–2.6; 2019–2050; MPI-ESM1-2-HR). (e-h) Future period (SSP5–8.5; 2019–2050; MPI-ESM1-2-HR). The barplot (b, d, f, h) represents the proportion of the contribution of each variable in the permafrost and non-permafrost areas with significantly increased $NDVI_{GS}$ from MPI-ESM1-2-HR.

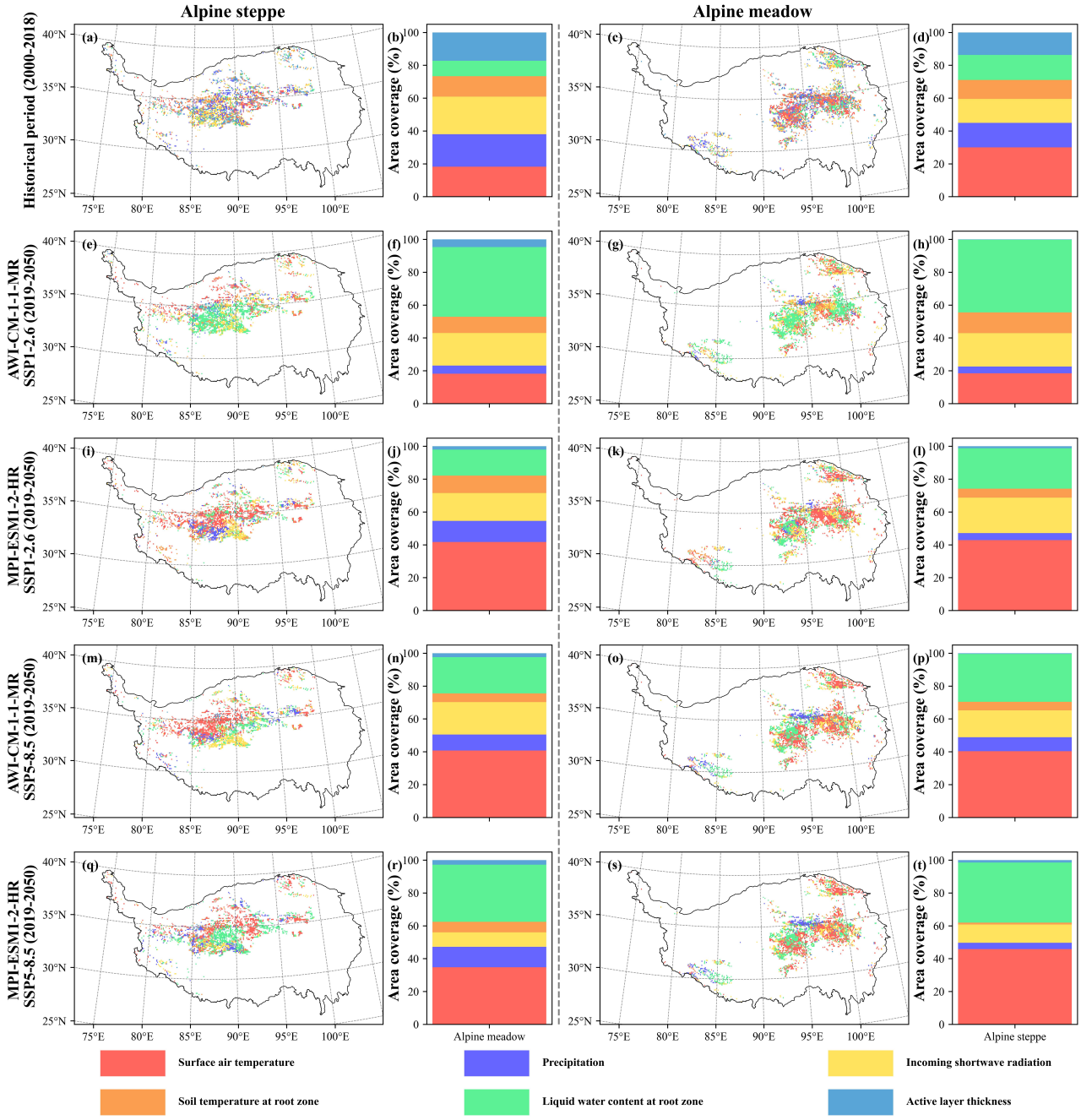


**Figure S8.** Spatial distribution of the dominant factors to the $NDVI_{GS}$ changes over different periods in the alpine meadow and alpine steppe over the permafrost areas. (a-d) Historical period (2000–2018). (e-h) Future period (SSP1–2.6; AWI-CM-1-1-MR). (i-l) Future period (SSP1–2.6; MPI-ESM1-2-HR). (m-p) Future period (SSP5–8.5; AWI-CM-1-1-MR). (q-t) Future period (SSP5–8.5; MPI-ESM1-2-HR). The barplot (b, d, f, h, j, l, n, p, r, t) represents the proportion of the contribution of each variable in the permafrost and non-permafrost with significantly increased $NDVI_{GS}$ from AWI-CM-1-1-MR and MPI-ESM1-2-HR.

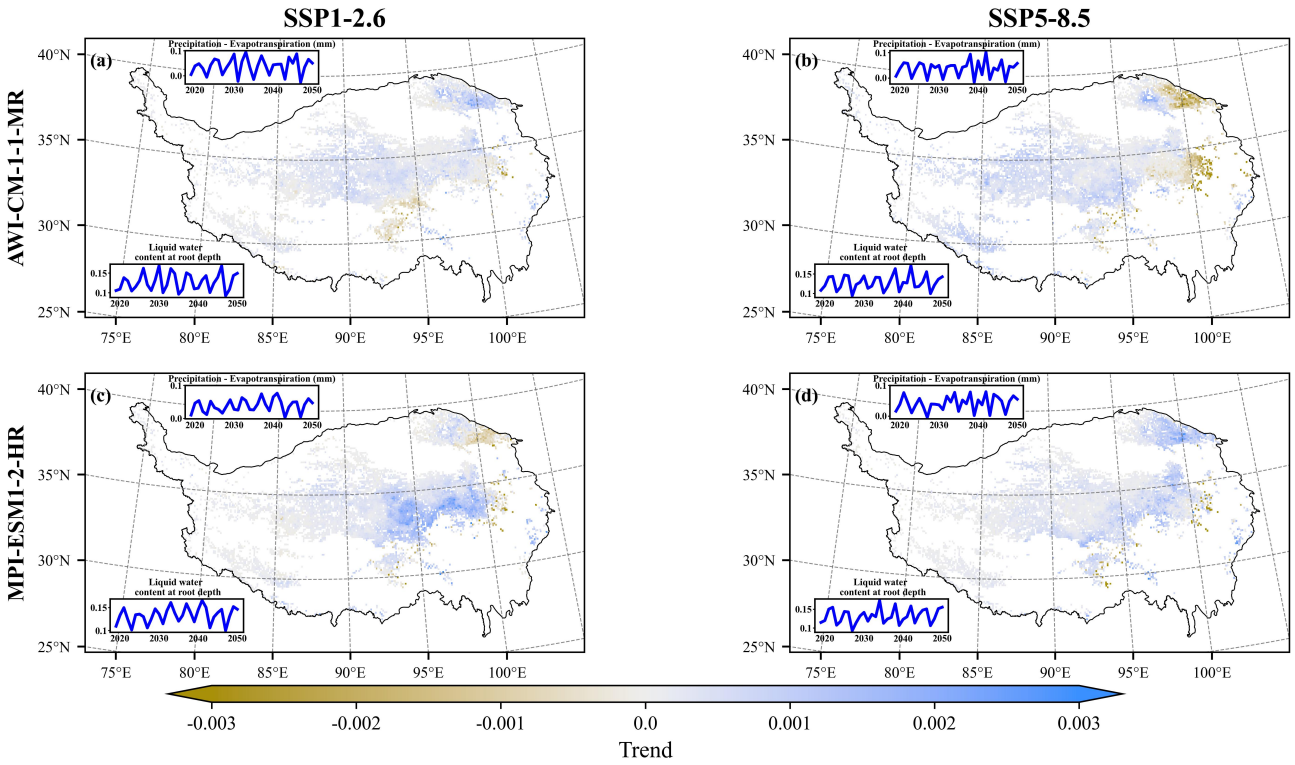


**Figure S9.** Spatiotemporal patterns of the changes of liquid water content at root zone across the permafrost areas during 2019–2050 under different scenarios. (a-b) AWI-CM-1-1-MR. (c-d) MPI-ESM1-2-HR. The line plots at each subplot indicate the time series of liquid water content at the root zone (bottom left) and precipitation minus evapotranspiration over the permafrost areas (top).

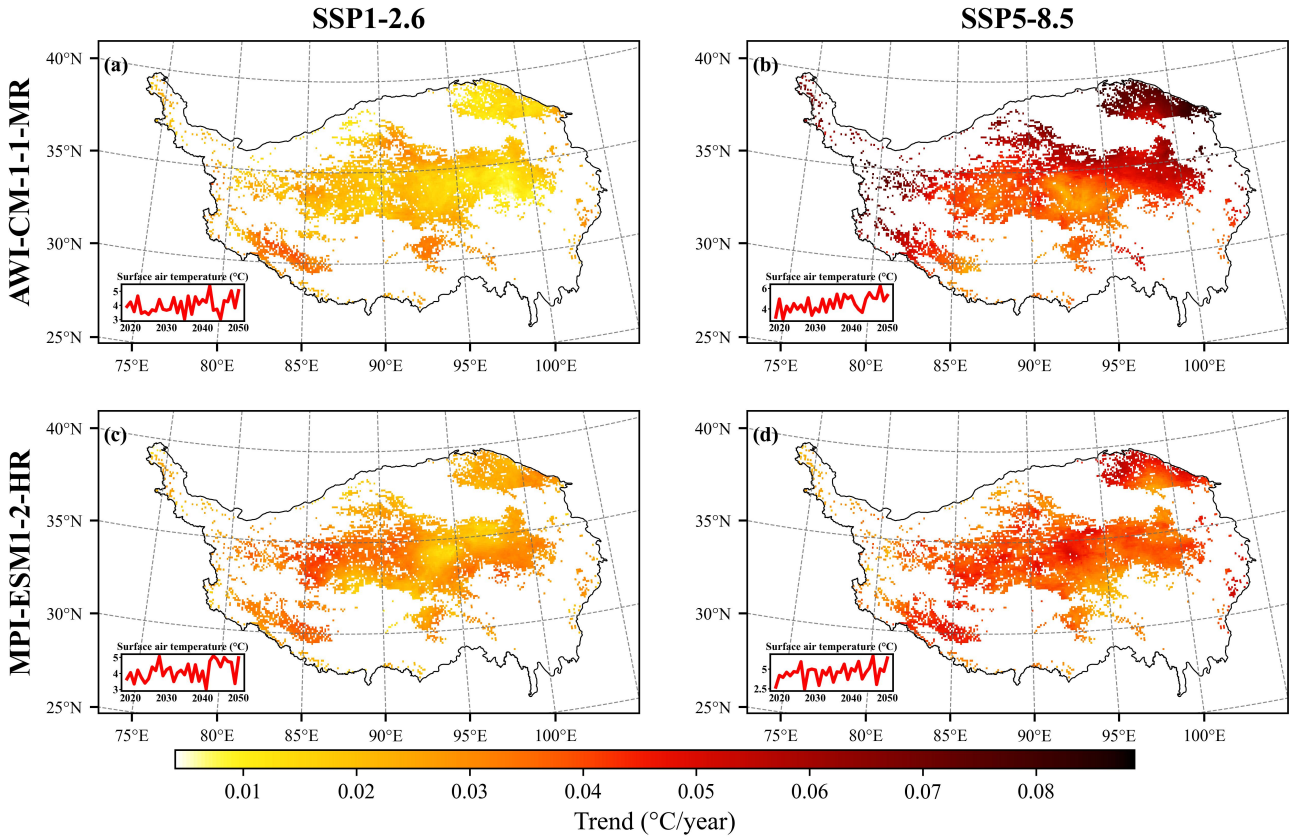


**Figure S10.** Spatiotemporal patterns of the changes of surface air temperature across the permafrost areas during 2019–2050 under different scenarios. (a-b) AWI-CM-1-1-MR. (c-d) MPI-ESM1-2-HR. The line plots at each subplot indicate the time series of surface air temperature.

**Table S1.** Overview of the CryoGridLite parameters used

| Parameter | Symbol | Value | Unit | Source |
|---|---|---|---|---|
| Natural constants | | | | |
| Atmospheric pressure at sea level | $P$ | $1.005\times10^{5}$ | Pa | — |
| Gravitational acceleration | $g$ | 9.81 | $\mathrm{m\,s^{-2}}$ | — |
| Von Kármán constant | $\kappa$ | 0.4 | — | — |
| Stefan-Boltzmann constant | $\sigma$ | $5.6704\times10^{-8}$ | $\mathrm{W\,m^{-2}\,K^{-4}}$ | — |
| Specific gas constant of air | $R$ | 287.058 | $\mathrm{J^{-1}\,kg^{-1}}$ | — |
| Surface properties | | | | |
| Albedo of fresh snow | $\alpha_{\mathrm{snow,max}}$ | 0.82 | — | Wang et al. (2020) |
| Albedo of old snow | $\alpha_{\mathrm{snow,min}}$ | 0.5 | — | Westermann et al. (2016) |
| Albedo of soil | $\alpha_{\mathrm{soil}}$ | 0.20 | — | Westermann et al. (2016) |
| Albedo of water surface | $\alpha_{\mathrm{water}}$ | 0.07 | — | Westermann et al. (2016) |
| Albedo of ice | $\alpha_{\mathrm{ice}}$ | 0.20 | — | Westermann et al. (2016) |
| Emissivity of snow | $\varepsilon_{\mathrm{snow}}$ | 0.99 | — | Westermann et al. (2016) |
| Emissivity of soil | $\varepsilon_{\mathrm{soil}}$ | 0.97 | — | Westermann et al. (2016) |
| Emissivity of water surface | $\varepsilon_{\mathrm{water}}$ | 0.99 | — | Westermann et al. (2016) |
| Emissivity of ice | $\varepsilon_{\mathrm{ice}}$ | 0.98 | — | Westermann et al. (2016) |
| Resistance at snow surface | $r_{\mathrm{s,snow}}$ | 0 | s m−1 | Westermann et al. (2016) |
| Resistance at soil surface | $r_{\mathrm{s,soil}}$ | 50 | s m−1 | Westermann et al. (2016) |
| Resistance at water surface | $r_{\mathrm{s,water}}$ | 0 | s m−1 | Westermann et al. (2016) |
| Resistance at ice surface | $r_{\mathrm{s,ice}}$ | 0 | s m−1 | Westermann et al. (2016) |
| Material properties | | | | |
| Density of snow | $\rho_{\mathrm{snow}}$ | 150 | $\mathrm{kg\,m^{-3}}$ | Dai, Che, Xie, and Wu (2018) |
| Density of water | $\rho_{\mathrm{water}}$ | 1000 | $\mathrm{kg\,m^{-3}}$ | Westermann et al. (2016) |
| Density of ice | $\rho_{\mathrm{ice}}$ | 1000 | $\mathrm{kg\,m^{-3}}$ | Westermann et al. (2016) |
| Density of air at sea level | $\rho_{\mathrm{air}}$ | 1.293 | $\mathrm{kg\,m^{-3}}$ | Westermann et al. (2016) |
| Evaporation Depth | $d_{\mathrm{E}}$ | 0.2 | m | — |
| Volumetric heat capacity of water | $C_{\mathrm{water}}$ | $4.2\times10^{6}$ | $\mathrm{J\,K^{-1}\,m^{-3}}$ | Westermann et al. (2016) |
| Volumetric heat capacity of ice | $C_{\mathrm{ice}}$ | $1.9\times10^{6}$ | $\mathrm{J\,K^{-1}\,m^{-3}}$ | Westermann et al. (2016) |
| Volumetric heat capacity of air | $C_{\mathrm{air}}$ | $1.25\times10^{3}$ | $\mathrm{J\,K^{-1}\,m^{-3}}$ | Westermann et al. (2016) |
| Volumetric heat capacity of mineral soil | $C_{\mathrm{minear}}$ | $2.0\times10^{6}$ | $\mathrm{J\,K^{-1}\,m^{-3}}$ | Westermann et al. (2016) |
| Volumetric heat capacity of organic soil | $C_{\mathrm{organic}}$ | $2.5\times10^{6}$ | $\mathrm{J\,K^{-1}\,m^{-3}}$ | Westermann et al. (2016) |
| Thermal conductivity of water | $k_{\mathrm{water}}$ | 0.57 | $\mathrm{W\,m^{-1}\,K^{-1}}$ | Westermann et al. (2016) |
| Thermal conductivity of ice | $k_{\mathrm{ice}}$ | 2.2 | $\mathrm{W\,m^{-1}\,K^{-1}}$ | Westermann et al. (2016) |
| Thermal conductivity of air | $k_{\mathrm{air}}$ | 0.025 | $\mathrm{W\,m^{-1}\,K^{-1}}$ | Westermann et al. (2016) |
| Thermal conductivity of mineral soil | $k_{\mathrm{mineral}}$ | 3.00 | $\mathrm{W\,m^{-1}\,K^{-1}}$ | Westermann et al. (2016) |
| Thermal conductivity of organic soil | $k_{\mathrm{organic}}$ | 0.25 | $\mathrm{W\,m^{-1}\,K^{-1}}$ | Westermann et al. (2016) |
| Specific latent heat of fusion water | $L_{\mathrm{sl}}$ | $0.334\times10^{6}$ | $\mathrm{J\,kg^{-1}}$ | Westermann et al. (2016) |
| Specific latent heat of vaporization | $L_{\mathrm{lg}}$ | $2.501\times10^{6}$ | $\mathrm{J\,kg^{-1}}$ | Westermann et al. (2016) |

**Table S2.** Overview of the hyperparameter settings for the different machine learning models

| Model | Hyperparameter | Searching space | Best parameter | |
|---|---|---|---|---|
| | | | permafrost | non-permafrost |
| LightGBM | n_estimators | [100, 2000] | 1850 | 1880 |
| | max_depth | [3, 20] | 19 | 20 |
| | learning_rate | [0.001, 0.3] | 0.062 | 0.069 |
| | num_leaves | [5, 1000] | 788 | 860 |
| | colsample_bytree | [0.4, 1] | 0.957 | 0.947 |
| | subsample | [0.4, 1] | 0.917 | 0.986 |
| | subsample_freq | [1, 7] | 4 | 4 |
| | min_child_samples | [5, 100] | 35 | 7 |
| | reg_alpha | [$1\times10^{-8}$, 10] | 0.108 | 1.037×10−6 |
| | reg_lambda | [$1\times10^{-8}$, 10] | 0.002 | $1.463\times10^{-6}$ |
| | max_bin | [255, 511] | 353 | 290 |
| XGBoost | n_estimators | [100, 2000] | 1395 | 1583 |
| | max_depth | [3, 15] | 15 | 15 |
| | learning_rate | [0.001, 0.3] | 0.015 | 0.019 |
| | min_child_weight | [1, 20] | 2 | 14 |
| | colsample_bytree | [0.4, 1] | 0.936 | 0.983 |
| | subsample | [0.4, 1] | 0.878 | 0.763 |
| | reg_alpha | [$1\times10^{-8}$, 10] | $1.425\times10^{-6}$ | $5.357\times10^{-8}$ |
| | reg_lambda | [$1\times10^{-8}$, 10] | $3.657\times10^{-4}$ | $2.977\times10^{-6}$ |
| | gamma | [$1\times10^{-8}$, 10] | $1.382\times10^{-6}$ | $5.202\times10^{-6}$ |

Note: Searching space of weight parameters for both models is from 1 to 100.

**Table S3.** Information on MAGT and ALT boreholes from 2000–2015 was used for validating the modeled results

| Variables | Sites | Lon (°E) | Lat (°N) | Altitude (m) | Reference/ Source | Sites | Longitude (°E) | Latitude (°N) | Altitude (m) | Reference/ Source |
|---|---|---|---|---|---|---|---|---|---|---|
| | K512 | 79.39 | 35.86 | 4766 | H. Chen et al. (2015) | YH | 70.40 | 35.77 | 4850 | H. Chen et al. (2015) |
| | K521 | 79.42 | 35.79 | 4928 | Qin et al. (2017) | K572 | 79.46 | 35.72 | 4690 | Qin et al. (2017) |
| | K529 | 79.46 | 35.72 | 4952 | H. Chen et al. (2015) | MPQT | 79.49 | 35.68 | 5175 | H. Chen et al. (2015) |
| | TSH | 79.55 | 35.36 | 4834 | H. Chen et al. (2015) | TSHGT | 79.55 | 35.36 | — | Zhao et al. (2021) |
| | K610 | 79.64 | 35.08 | 4926 | Qin et al. (2017) | SLMC | 80.39 | 34.56 | 5050 | H. Chen et al. (2015) |
| | LN2 | 80.39 | 34.63 | 5001 | Qin et al. (2017) | NLMC | 80.39 | 34.64 | 5016 | H. Chen et al. (2015) |
| | MPJS | 80.42 | 34.54 | 5117 | H. Chen et al. (2015) | LZL | 81.33 | 34.80 | 5009 | H. Chen et al. (2015) |
| | LZL3 | 81.33 | 34.81 | 5009 | Qin et al. (2017) | DLSW | 84.18 | 33.00 | 4919 | Qin et al. (2017) |
| | NO.GZ | 85.13 | 33.80 | 4990 | Qin et al. (2017) | GM | 85.63 | 33.39 | 5095 | Qin et al. (2017) |
| | FCKGT | 88.57 | 37.46 | — | Zhao et al. (2021) | STG | 88.60 | 37.58 | 4500 | Qin et al. (2017) |
| | AYK2 | 88.61 | 37.52 | 4645 | Qin et al. (2017) | AYKGT | 88.61 | 37.52 | — | Zhao et al. (2021) |
| | AYK3 | 88.70 | 37.51 | 4500 | Qin et al. (2017) | NO.72 | 91.40 | 33.01 | 4930 | Qin et al. (2017) |
| | AD2 | 91.58 | 32.31 | 4814 | Q. Wu et al. (2020) | NO.39 | 91.53 | 32.42 | 4995 | Qin et al. (2017) |
| | TJ1 | 91.53 | 32.51 | 4868 | Q. Wu et al. (2020) | TJ2 | 91.62 | 32.39 | 4887 | Q. Wu et al. (2020) |
| | QTB18 | 91.74 | 31.82 | — | Zhao et al. (2021) | TG4 | 91.75 | 33.07 | 4974 | Q. Wu et al. (2020) |
| | ZNHW | 91.86 | 35.49 | 4768 | Qin et al. (2017) | TG3 | 91.80 | 33.09 | 4926 | Q. Wu et al. (2020) |
| | TG2 | 91.87 | 33.30 | 4841 | Q. Wu et al. (2020) | WQ | 91.90 | 33.10 | 4960 | Qin et al. (2017) |
| | TGLGT | 91.94 | 33.07 | — | Zhao et al. (2021) | WQ1 | 91.94 | 33.47 | 4778 | Q. Wu et al. (2020) |
| | WQ2 | 91.95 | 33.40 | 4817 | Q. Wu et al. (2020) | ZNHGT | 91.96 | 35.49 | — | Zhao et al. (2021) |
| | ZNH5 | 91.96 | 35.49 | 4784 | Qin et al. (2017) | NO.64 | 92.14 | 33.46 | 4620 | Qin et al. (2017) |
| | No.62 | 92.20 | 34.01 | 4680 | Qin et al. (2017) | NO.61 | 92.26 | 34.13 | 4550 | Qin et al. (2017) |
| | KKXL1 | 92.28 | 35.53 | 4701 | Qin et al. (2017) | TT2 | 92.20 | 33.76 | 4647 | Q. Wu et al. (2020) |
| | TT1 | 92.23 | 33.88 | 4640 | Q. Wu et al. (2020) | KL1 | 92.34 | 34.01 | 4672 | Q. Wu et al. (2020) |
| | KL3 | 92.34 | 33.96 | 4622 | Q. Wu et al. (2020) | KL5 | 92.34 | 33.94 | 4622 | Q. Wu et al. (2020) |
| | NO.59 | 92.44 | 34.29 | 4579 | Qin et al. (2017) | NO.34 | 92.44 | 34.29 | 4583 | Qin et al. (2017) |
| | NO.56 | 92.47 | 34.37 | 4714 | Qin et al. (2017) | NO.32 | 92.56 | 34.49 | 4634 | Qin et al. (2017) |
| | NO.31 | 92.57 | 34.51 | 4595 | Qin et al. (2017) | QTB11 | 92.66 | 34.39 | — | Zhao et al. (2021) |
| | YM2 | 92.73 | 34.53 | 4616 | Q. Wu et al. (2020) | YM1 | 92.74 | 34.58 | 4654 | Q. Wu et al. (2020) |
| MAGT | WL1 | 92.73 | 34.48 | 4587 | Q. Wu et al. (2020) | FH3 | 92.78 | 34.61 | 4715 | Q. Wu et al. (2020) |
| | FH2 | 92.90 | 34.67 | 4894 | Q. Wu et al. (2020) | NO.11 | 92.93 | 34.82 | 4637 | Qin et al. (2017) |
| | NO.9 | 92.95 | 34.85 | 4592 | Qin et al. (2017) | KKXL3 | 92.96 | 35.48 | 4554 | Qin et al. (2017) |
| | NO.54 | 93.02 | 35.04 | 4570 | Qin et al. (2017) | NO.53 | 93.03 | 35.08 | 4731 | Qin et al. (2017) |
| | NO.52 | 93.07 | 35.12 | 4610 | Qin et al. (2017) | NO.4 | 93.07 | 35.21 | 4635 | Qin et al. (2017) |
| | HR3 | 93.03 | 35.07 | 4675 | Q. Wu et al. (2020) | WD4 | 93.04 | 35.14 | 4734 | Q. Wu et al. (2020) |
| | QTB09 | 93.03 | 35.13 | — | Zhao et al. (2021) | QTB08 | 93.08 | 35.22 | — | Zhao et al. (2021) |
| | WD3 | 93.11 | 35.20 | 4613 | Q. Wu et al. (2020) | NO.50 | 93.27 | 35.22 | 4510 | Qin et al. (2017) |
| | CM7 | 93.22 | 35.28 | 4589 | Q. Wu et al. (2020) | QTB06 | 93.27 | 35.29 | — | Zhao et al. (2021) |
| | NO.27 | 93.32 | 35.24 | 4487 | Qin et al. (2017) | NO.21 | 93.45 | 35.31 | 4568 | Qin et al. (2017) |
| | CM5 | 93.45 | 35.36 | 4507 | Q. Wu et al. (2020) | CM6 | 93.45 | 35.36 | 4504 | Q. Wu et al. (2020) |
| | QTB05 | 93.45 | 35.36 | — | Zhao et al. (2021) | NO.46 | 93.58 | 35.33 | 4640 | Qin et al. (2017) |
| | NO.66 | 93.78 | 35.52 | 4560 | Qin et al. (2017) | QTB03 | 93.78 | 35.52 | — | Zhao et al. (2021) |
| | CM3 | 93.96 | 35.55 | 4547 | Q. Wu et al. (2020) | BD1 | 93.96 | 35.62 | 4636 | Q. Wu et al. (2020) |
| | KLS | 94.06 | 35.63 | 4753 | Qin et al. (2017) | KM2 | 94.05 | 35.62 | 4757 | Q. Wu et al. (2020) |
| | QTB02 | 94.06 | 35.63 | — | Zhao et al. (2021) | QTB01 | 94.08 | 35.72 | — | Zhao et al. (2021) |
| | XDTGT | 94.13 | 35.72 | — | Zhao et al. (2021) | QSH-1 | 97.15 | 33.78 | 4413 | Luo et al. (2018) |
| | QSH-2 | 97.17 | 33.74 | 4395 | Luo et al. (2018) | QSH-3 | 97.17 | 33.74 | 4403 | Luo et al. (2018) |
| | K634–1 | 97.38 | 33.98 | 4532 | Luo et al. (2018) | K634–2 | 97.38 | 33.98 | 4536 | Luo et al. (2018) |
| | CLQ-1 | 97.56 | 34.04 | 4634 | Luo et al. (2018) | CLQ-2 | 97.57 | 34.04 | 4614 | Luo et al. (2018) |
| | BSKN | 97.65 | 34.11 | 4744 | Luo et al. (2018) | BSK | 97.66 | 34.13 | 4833 | Luo et al. (2018) |
| | CLP3 | 97.87 | 34.27 | 4663 | Qin et al. (2017) | CLP-1 | 97.85 | 34.26 | 4721 | Luo et al. (2018) |
| | CLP-2 | 97.85 | 34.26 | 4724 | Luo et al. (2018) | CLP-3 | 97.87 | 34.27 | 4663 | Luo et al. (2018) |
| | CLP4 | 97.90 | 34.31 | 4564 | Qin et al. (2017) | YNG1 | 97.95 | 34.40 | 4452 | Qin et al. (2017) |
| | NO.YNP3 | 97.97 | 34.50 | 4333 | Qin et al. (2017) | CLP-4 | 97.90 | 34.31 | 4564 | Luo et al. (2018) |
| | YNG-1 | 97.95 | 34.40 | 4446 | Luo et al. (2018) | YNG-2 | 97.94 | 34.44 | 4395 | Luo et al. (2018) |
| | YNG-3 | 97.97 | 34.50 | 4324 | Luo et al. (2018) | MDB | 98.44 | 34.85 | 4225 | Luo et al. (2018) |
| | K445 | 98.55 | 34.97 | 4282 | Luo et al. (2018) | ZK3 | 99.15 | 35.37 | 4228 | Qin et al. (2017) |
| | ZK21 | 99.56 | 35.40 | 4602 | Qin et al. (2017) | | | | | |
| | K512 | 79.39 | 35.86 | 4766 | H. Chen et al. (2015) | YH | 70.40 | 35.77 | 4850 | H. Chen et al. (2015) |
| | K529 | 79.46 | 35.72 | 4952 | H. Chen et al. (2015) | MPQT | 79.49 | 35.68 | 5175 | H. Chen et al. (2015) |
| | TSH | 79.55 | 35.36 | 4834 | H. Chen et al. (2015) | SLMC | 80.39 | 34.56 | 5050 | H. Chen et al. (2015) |
| | NLMC | 80.39 | 34.64 | 5016 | H. Chen et al. (2015) | MPJS | 80.42 | 34.54 | 5117 | H. Chen et al. (2015) |
| | LZL | 81.33 | 34.80 | 5009 | H. Chen et al. (2015) | AD2 | 91.58 | 32.31 | 4814 | Q. Wu et al. (2020) |
| | TJ1 | 91.53 | 32.51 | 4868 | Q. Wu et al. (2020) | TJ2 | 91.62 | 32.39 | 4887 | Q. Wu et al. (2020) |
| | TG4 | 91.75 | 33.07 | 4974 | Q. Wu et al. (2020) | TG3 | 91.80 | 33.09 | 4926 | Q. Wu et al. (2020) |
| | TG2 | 91.87 | 33.30 | 4841 | Q. Wu et al. (2020) | WQ1 | 91.94 | 33.47 | 4778 | Q. Wu et al. (2020) |
| | WQ2 | 91.95 | 33.40 | 4817 | Q. Wu et al. (2020) | TT1 | 92.23 | 33.88 | 4640 | Q. Wu et al. (2020) |
| | TT1 | 92.23 | 33.88 | 4640 | Z. Zhang et al. (2020) | CLP1 | 92.35 | 33.96 | 4627 | Qin et al. (2017) |
| | KL1 | 92.34 | 34.01 | 4672 | Q. Wu et al. (2020) | KL3 | 92.34 | 33.96 | 4622 | Q. Wu et al. (2020) |
| | KL5 | 92.34 | 33.94 | 4622 | Q. Wu et al. (2020) | KL3 | 92.34 | 33.96 | 4672 | Z. Zhang et al. (2020) |
| | YM2 | 92.73 | 34.53 | 4616 | Q. Wu et al. (2020) | YM1 | 92.74 | 34.58 | 4654 | Q. Wu et al. (2020) |
| | WL1 | 92.73 | 34.48 | 4587 | Q. Wu et al. (2020) | FH3 | 92.78 | 34.61 | 4715 | Q. Wu et al. (2020) |
| | FHS1 | 98.89 | 34.73 | 4896 | Qin et al. (2017) | FH2 | 92.90 | 34.67 | 4894 | Q. Wu et al. (2020) |
| | BLR1 | 92.92 | 34.86 | 4633 | Qin et al. (2017) | BL1 | 92.93 | 34.83 | 4635 | Z. Zhang et al. (2020) |
| | FH4 | 92.90 | 34.68 | 4992 | Z. Zhang et al. (2020) | WD4 | 93.04 | 35.14 | 4734 | Q. Wu et al. (2020) |
| | HR3 | 93.03 | 35.07 | 4675 | Q. Wu et al. (2020) | WD4 | 93.04 | 35.14 | 4734 | Z. Zhang et al. (2020) |
| | WD3 | 93.11 | 35.20 | 4613 | Q. Wu et al. (2020) | CM7 | 93.22 | 35.28 | 4589 | Q. Wu et al. (2020) |
| ALT | CM5 | 93.45 | 35.36 | 4507 | Q. Wu et al. (2020) | CM6 | 93.45 | 35.36 | 4504 | Q. Wu et al. (2020) |
| | CM5 | 93.45 | 35.36 | 4507 | Z. Zhang et al. (2020) | KKXL | 93.60 | 35.45 | 4488 | Qin et al. (2017) |
| | BD1 | 93.96 | 35.62 | 4636 | Q. Wu et al. (2020) | CM3 | 93.96 | 35.55 | 4547 | Q. Wu et al. (2020) |
| | S308_5 | 94.07 | 35.08 | 4512 | Qin et al. (2017) | XDT2 | 94.09 | 35.71 | 4530 | Qin et al. (2017) |
| | XDT1 | 94.04 | 35.71 | 4602 | Qin et al. (2017) | KM2 | 94.05 | 35.62 | 4757 | Q. Wu et al. (2020) |
| | ZD | 94.40 | 32.82 | 4775 | Qin et al. (2017) | S308_4 | 94.79 | 34.90 | 4475 | Qin et al. (2017) |
| | S308_3 | 95.19 | 34.68 | 4661 | Qin et al. (2017) | S308_2 | 95.97 | 34.16 | 4733 | Qin et al. (2017) |
| | S308_1 | 96.96 | 33.77 | 4676 | Qin et al. (2017) | ZLH2 | 97.31 | 34.69 | 4402 | Qin et al. (2017) |
| | GST-51 | 97.38 | 33.98 | 4532 | Gao et al. (2023) | GST-49 | 97.38 | 33.98 | 4536 | Gao et al. (2023) |
| | GST-7 | 97.57 | 35.01 | 4299 | Gao et al. (2023) | GST-6 | 97.58 | 35.02 | 4299 | Gao et al. (2023) |
| | GST-46 | 97.65 | 34.11 | 4749 | Gao et al. (2023) | CLP2 | 97.85 | 34.26 | 4717 | Qin et al. (2017) |
| | GST-37 | 97.85 | 34.26 | 4724 | Gao et al. (2023) | GST-31 | 97.87 | 34.27 | 4663 | Gao et al. (2023) |
| | GST-8 | 98.44 | 34.85 | 4219 | Gao et al. (2023) | PT1 | 98.75 | 38.78 | 4128 | Mu and Peng (2022) |
| | PT2 | 98.78 | 38.83 | 3985 | Mu and Peng (2022) | PT3 | 98.85 | 38.84 | 3827 | Mu and Peng (2022) |
| | PT4 | 98.95 | 38.83 | 3770 | Mu and Peng (2022) | PT5 | 99.03 | 38.81 | 3691 | Mu and Peng (2022) |
| | PT6 | 98.96 | 38.95 | 4153 | Mu and Peng (2022) | PT7 | 98.96 | 38.90 | 3970 | Mu and Peng (2022) |
| | PT10 | 99.07 | 38.79 | 3681 | Mu and Peng (2022) | Ebo TA | 100.92 | 38.00 | 3691 | Mu and Peng (2022) |
| | Ebo TB | 100.91 | 38.00 | 3615 | Mu and Peng (2022) | KHW | 99.15 | 35.36 | 4166 | Qin et al. (2017) |
| | KHE | 99.28 | 35.33 | 4338 | Qin et al. (2017) | JLLW | 99.33 | 35.40 | 4324 | Qin et al. (2017) |
| | ELS | 99.50 | 35.49 | 4330 | Qin et al. (2017) | ZK21 | 85.13 | 33.80 | 5020 | J. Chen et al. (2016) |
| | ZK13 | 85.31 | 33.18 | 5120 | J. Chen et al. (2016) | ZK14 | 85.35 | 33.21 | 5130 | J. Chen et al. (2016) |
| | ZK18 | 85.36 | 33.39 | 5120 | J. Chen et al. (2016) | ZK15 | 85.63 | 33.39 | 5130 | J. Chen et al. (2016) |
| | ZK16 | 85.63 | 33.39 | 5120 | J. Chen et al. (2016) | ZK17 | 85.63 | 33.39 | 5120 | J. Chen et al. (2016) |
| | ZK19 | 85.65 | 33.35 | 5050 | J. Chen et al. (2016) | ZK22 | 85.63 | 33.39 | 5120 | J. Chen et al. (2016) |

**Table S4.** Comparison of observed and modeled soil temperature at 0–40cm depth.

| Sites | Longitude (° E) | Latitude (° N) | Altitude (m) | Period | Observation (° $C$) | | Simulation (° $C$) | | Bias (° $C$) |
|---|---|---|---|---|---|---|---|---|---|
| | | | | | Mean | Std | Mean | Std | |
| 51886 | 90.85 | 38.25 | 2945 | 1988–2012 | 8.3 | 11.4 | 9.8 | 11.3 | -1.5 |
| 52602 | 93.33 | 38.75 | 2770 | 1980–2012 | 7.6 | 11.5 | 8.5 | 11.8 | -0.9 |
| 52633 | 98.42 | 38.80 | 3367 | 2004–2012 | 2.5 | 9.2 | 2.1 | 8.9 | 0.4 |
| 52657 | 100.25 | 38.18 | 2787 | 2004–2012 | 5.8 | 9.7 | 3.5 | 9.4 | 2.3 |
| 52707 | 93.68 | 36.80 | 2767 | 2004–2012 | 9.8 | 10.6 | 10.5 | 11.3 | -0.7 |
| 52713 | 95.37 | 37.85 | 3173 | 2004–2012 | 8.6 | 11.1 | 9.0 | 12.0 | -0.4 |
| 52737 | 97.37 | 37.37 | 2982 | 1980–2012 | 7.2 | 10.1 | 9.6 | 11.3 | -2.4 |
| 52754 | 100.13 | 37.33 | 3345 | 1980–2012 | 3.6 | 8.0 | 2.9 | 8.3 | 0.7 |
| 52765 | 101.62 | 37.38 | 2938 | 1982–2012 | 4.6 | 8.2 | 4.0 | 9.3 | 0.6 |
| 52825 | 96.42 | 36.43 | 2790 | 2004–2012 | 9.2 | 11.3 | 12.6 | 11.8 | -3.4 |
| 52833 | 98.48 | 36.92 | 2950 | 2004–2012 | 8.0 | 10.2 | 8.2 | 10.9 | -0.2 |
| 52836 | 98.10 | 36.30 | 3191 | 2004–2012 | 6.6 | 9.1 | 7.3 | 10.4 | -0.7 |
| 52856 | 100.62 | 36.27 | 2835 | 1982–2012 | 7.9 | 9.4 | 9.4 | 9.8 | -1.5 |
| 52943 | 99.98 | 35.58 | 3323 | 1992–2012 | 5.5 | 8.1 | 7.5 | 8.6 | -2.0 |
| 52955 | 100.75 | 35.58 | 3203 | 2004–2012 | 6.2 | 9.1 | 6.4 | 9.0 | -0.2 |
| 52974 | 102.02 | 35.52 | 2491 | 2004–2012 | 9.1 | 8.7 | 11.1 | 9.0 | -2.0 |
| 55228 | 79.59 | 32.11 | 4279 | 1994–2012 | 6.8 | 10.8 | 5.6 | 10.8 | 1.2 |
| 55248 | 84.25 | 32.09 | 4415 | 2007–2012 | 5.5 | 8.9 | 7.8 | 9.7 | -2.3 |
| 55279 | 89.40 | 31.48 | 4700 | 2007–2012 | 4.6 | 7.0 | 5.3 | 7.8 | -0.7 |
| 55294 | 91.06 | 32.21 | 4800 | 2006–2012 | 3.3 | 7.5 | 4.0 | 7.3 | -0.7 |
| 55299 | 92.16 | 32.06 | 4507 | 2006-2012 | 4.8 | 7.0 | -0.5 | 5.5 | 5.3 |
| 55437 | 81.15 | 30.17 | 4900 | 1994–2012 | 10.4 | 8.8 | 6.7 | 9.2 | 3.7 |
| 55472 | 83.8 | 30.57 | 4672 | 2007–2012 | 5.4 | 8.2 | 1.7 | 7.3 | 2.7 |
| 55493 | 91.05 | 30.29 | 4200 | 2006–2012 | 7.7 | 7.2 | 7.1 | 7.5 | 0.6 |
| 55569 | 87.38 | 29.05 | 4000 | 2007–2012 | 11.9 | 7.2 | 6.1 | 7.5 | 5.8 |
| 56021 | 95.78 | 34.13 | 4175 | 1982–2012 | 3.1 | 7.7 | 2.7 | 7.8 | 0.4 |
| 56029 | 97.02 | 33.02 | 3681 | 2004–2012 | 7.3 | 7.5 | 6.8 | 8.0 | 0.5 |
| 56033 | 98.22 | 34.92 | 4272 | 1980–2012 | 1.5 | 7.6 | -0.9 | 8.6 | 2.4 |
| 56034 | 97.13 | 33.80 | 4415 | 2004–2012 | 1.5 | 6.5 | -0.4 | 7.1 | 1.9 |
| 56043 | 100.25 | 34.47 | 3719 | 2004–2012 | 4.5 | 7.3 | 4.6 | 6.3 | -0.1 |
| 56065 | 101.60 | 34.73 | 3670 | 1981–2012 | 3.9 | 7.0 | 3.0 | 8.4 | 0.9 |
| 56125 | 96.48 | 32.20 | 3644 | 1993–2012 | 8.6 | 7.3 | 6.8 | 7.9 | 1.8 |
| 56151 | 100.75 | 32.93 | 3530 | 2004–2012 | 7.2 | 7.1 | 5.5 | 7.7 | 1.7 |
| 56434 | 97.28 | 28.39 | 2328 | 2007–2012 | 15.0 | 5.9 | 7.4 | 4.9 | 7.6 |
| S6 | 89.47 | 28.30 | 4450 | 2018 | 4.9 | 7.4 | 6.8 | 5.9 | -1.9 |
| S9 | 94.43 | 29.54 | 2992 | 2018 | 10.1 | 6.2 | 13.5 | 5.2 | -3.4 |

Note: Study sites were selected based on their location and the observational periods. These sites need to be located in our model domain and within the period of historical simulation. Data derived from Cuo, Zhang, and Li (2022).

**Table S5.** Comparison of the average thermal state permafrost and active layer thickness over the Tibetan Plateau between this study and other research

| Variables | Historical period | Mid-century | | | | End-century | | | | Methods | Reference |
|---|---|---|---|---|---|---|---|---|---|---|---|
| | | SSP1-2.6 /RCP2.6 | SSP2-4.5 /RCP4.5 | SSP3-7.0 /RCP7.0 | SSP5-8.5 /RCP8.5 | SSP1-2.6 /RCP2.6 | SSP2-4.5 /RCP4.5 | SSP3-7.0 /RCP6.0 | SSP5-8.5 /RCP8.5 | | |
| MAGT ($^{\circ}C$) | **-2.26±0.17** | **-2.33±0.20** | — | — | **-1.98±0.17** | **-2.52±0.18** | — | — | **-1.06±0.12** | **TNM** | **this study** |
| | -1.35±0.42 | — | — | — | — | -0.66 | -0.14 | — | 0.25 | ML | Ni et al. (2021) |
| | -1.56 | — | — | — | — | — | — | — | — | TNM | X. Wu et al. (2018) |
| | -1.72 | -0.43 | -0.17 | 0.02 | 0.33 | -0.43 | 0.65 | 1.93 | 2.96 | ML&EQM | Ran et al. (2022) |
| | -3.32 | — | — | — | — | — | -2.52 | -1.32 | -0.72 | TNM | G. Zhang et al. (2022) |
| ALT (m) | **3.04±0.09** | **3.07±0.18** | — | — | **3.41±0.19** | **2.80±0.14** | — | — | **4.91±0.29** | **TNM** | **this study** |
| | 2.01 | — | — | — | — | — | — | — | — | TNM | Guo and Wang (2013) |
| | 2.30±0.60 | — | — | — | — | 2.50 | 2.50 | — | 2.70 | ML | Ni et al. (2021) |
| | 3.23 | — | — | — | — | — | — | — | — | TNM | X. Wu et al. (2018) |
| | 2.46 | — | — | — | — | — | — | — | — | EQM | Xu and Wu (2021) |
| | 1.35±0.33 | — | — | — | — | — | — | — | — | TNM | Yin et al. (2021) |
| | 2.11 | 2.65 | 2.74 | 2.80 | 2.90 | 2.65 | 3.00 | 3.42 | 3.73 | ML&EQM | Ran et al. (2022) |
| | 1.24 | — | — | — | — | — | 1.94 | 2.74 | 4.24 | TNM | G. Zhang et al. (2022) |
| | 2.54 | — | — | — | — | 2.78 | 2.95 | — | 3.91 | EQM | Ji et al. (2022) |
| | 2.43 | — | — | — | — | — | — | — | — | ML | R. Li et al. (2023) |
| | 2.39 | — | — | — | — | — | — | — | — | ML&EQM | Shen et al. (2023) |
| PA ($\times 10^6 km^2$) | **1.10±0.02** | **0.96±0.03** | — | — | **0.92±0.04** | **0.88±0.04** | — | — | **0.59±0.06** | **TNM** | **this study** |
| | 1.52 | | | | | | | | | TNM | Guo and Wang (2013) |
| | 1.24±0.03 | — | — | — | — | 0.67±0.13 | 0.40±0.11 | 0.34±0.12 | 0.09±0.06 | EQM | Guo and Wang (2016) |
| | 1.48 | 1.09 | 0.96 | 0.96 | 0.78 | 1.10 | 0.88 | 0.80 | 0.55 | EQM | W. Zhang et al. (2016) |
| | 1.66 | 1.26 | 1.12 | 1.21 | 0.97 | 1.29 | 0.93 | 0.89 | 0.59 | EQM | Lu et al. (2017) |
| | 1.06 | | | | | | | | | EQM | Zou et al. (2017) |
| | 1.27 | 1.06 | 1.01 | 1.12 | 0.93 | 1.06 | 0.85 | 0.87 | 0.53 | EQM | Chang et al. (2018) |
| | 1.29 | — | — | — | — | — | — | — | — | TNM | X. Wu et al. (2018) |
| | 1.11 | — | — | — | — | — | — | — | — | EQM | Ran et al. (2018) |
| | 1.04 | — | — | — | — | 0.91 | 0.62 | — | 0.44 | ML | Ni et al. (2021) |
| | 1.15 | — | — | — | — | — | — | — | — | ML | Ran et al. (2021) |
| | 1.42 | — | — | — | — | 1.04 | 0.57 | — | 0.28 | TNM | Yin et al. (2021) |
| | 1.01 | — | — | — | — | — | — | — | — | ML&EQM | Ran et al. (2022) |
| | 1.07 | 0.85 | 0.85 | 0.83 | 0.79 | 0.77 | 0.60 | 0.44 | 0.31 | TNM | G. Zhang et al. (2022) |
| | 1.34 | — | — | — | — | — | — | — | — | ML | R. Li et al. (2023) |
| | 1.04 | — | — | — | — | — | — | — | — | ML&EQM | Shen et al. (2023) |
| | 1.21±0.02 | 0.81±0.04 | 0.72±0.04 | 0.68±0.04 | 0.57±0.05 | 0.76±0.05 | 0.44±0.06 | 0.14±0.04 | 0.04±0.03 | EQM | H. Li et al. (2024) |

Note: The abbreviations MAGT, ALT, PA, TNM, EQM, and ML refer to mean annual ground temperature, active layer thickness, permafrost areas, transient numerical model, empirical equilibrium model, and machine learning algorithm, respectively. This study defines the historical period (2000–2018), mid-century (2041–2060), and end-century (2081–2100). Different studies have various definitions.